Acta Cryst. (1991). A47, 282-290

Characterization of the Densification of Alumina by Multiple Small-Angle Neutron Scattering

BY S. KRUEGER AND G. G. LONG

National Institute of Standards and Technology, Gaithersburg, MD 20899, *USA*

AND R. A. PAGE

Southwest Research Institute, San Antonio, TX 78228, *USA*

(*Received* 15 *July* 1990; *accepted* 4 *January* 1991)

Abstract

Multiple small-angle neutron scattering was used to follow the evolution of the pore-size distribution in α-Al_2O_3 through the intermediate and final stages of sintering. This new technique enables the study of microstructure in the 0·08–10 μm size regime, which is the size range of importance for many materials systems, without needing to increase the resolution of currently available small-angle scattering instruments. The microstructure evolution results indicate a nearly constant effective pore radius for the alumina throughout the intermediate sintering stage, ranging from 0·19 μm at 54% of theoretical density to 0·17 μm at 79% dense. As the alumina densifies further, there is a transition region after which the effective pore radius grows rapidly to ≥0·6 μm at 97·5% dense.

1. Introduction

Small-angle neutron scattering (SANS) is an important technique for the statistically significant evaluation of bulk microstructural parameters in materials containing dilute concentrations [where 'dilute' is represented by $\varphi/(1-\varphi) \sim \varphi$ and φ is the scattering volume fraction] of scatterers between 10 and 1000 Å. However, the relevant structures in many physical systems, such as partially sintered ceramics, cannot readily be studied by SANS since the usual approximations are not valid for the larger sizes and more-dense structures present in these materials. To perform neutron scattering characterization of high technology materials as a function of thermal processing, it has become increasingly important to extend the range of particle-size determinations usually associated with SANS up to ~10 μm and to be able to include the analysis of thicker and less-dilute $[\varphi/(1-\varphi) > \varphi]$ systems in which the coherent elastic differential scattering cross section is dominated by multiple scattering. These issues have been successfully addressed by the multiple small-angle neutron-scattering (MSANS) formalism of Berk & Hardman-Rhyne (1985, 1988), which applies when multiple scattering arises solely from the compounding of single-particle scattering events, meaning that there is no scattering component due to correlations between particles. Berk & Hardman-Rhyne refer to this type of scattering process as 'incoherent multiple scattering'.

The central assumptions of the MSANS formalism are that the observed MSANS intensity is the result of incoherent multiple scattering from a randomly distributed monodisperse population of spheres comprised of material of uniform density (*i.e.* containing no internal structure) and that the phase shift ν that a plane wave undergoes in traversing a particle of radius R is within the range ~0·1 to 2. Effective (volume-weighted average) radii of the scatterers are extracted by measuring the wavelength dependence of the broadening of the scattering curves.

An earlier study of microstructure evolution in porous silica as a function of thermal processing (Long & Krueger, 1989) demonstrated that MSANS and SANS can effectively be used together to cover the full range of relevant microstructure sizes. In this work, MSANS was used to follow the evolution of the pore-size distribution in α-Al_2O_3 through the intermediate and final stages of sintering.

Knowledge of the microstructure evolution as a function of thermal processing is important for the development of process models in ceramics. The process models for both the silica (Kingery & Berg, 1955) and alumina (Coble, 1961) systems are comparatively well understood. Whereas porous silica is a glassy system which sinters by means of viscous flow, alumina is a polycrystalline system which sinters by means of volume and surface diffusion. The different sintering mechanisms should give rise to different microstructure evolution. Thus, these well characterized materials can serve as model systems for the new MSANS technique.

2. MSANS theory

The interaction of neutrons with matter is characterized by the phase shift ν that a plane wave undergoes in traversing a particle of radius R. This phase shift

0108-7673/91/030282-09$03.00

determines the shape of the single-particle differential scattering cross section, $d\Sigma(Q)/d\Omega$, as a function of the scattering wavevector $\mathbf{Q}$, where $|Q| = 2\pi\varepsilon/\lambda$ and $\varepsilon \ll 1$ is the scattering angle. ν depends upon $\Delta\rho$, the contrast of the particle or void, relative to the scattering matrix such that

$$\nu = 2\Delta\rho R\lambda, \tag{1}$$

where $\Delta\rho$ is written as

$$\Delta\rho = \sum_{\text{cell}} (b_i/V) - \rho_{\text{matrix}}. \tag{2}$$

The b_i are the *coherent* scattering lengths of the individual nuclei whereas ρ_{matrix} is the average scattering-length density of the matrix. Thus, the phase shift is directly dependent upon the material contrast ($\Delta\rho$), the dimension of the scattering particle or void ($2R$) and the neutron wavelength (λ).

If $\nu \ll 1$ (the usual SANS diffraction regime), the measured scattered intensity can be described by the Born approximation (Porod, 1951; Weiss, 1951) of scattering theory or the Rayleigh–Gans model (Rayleigh, 1910, 1914; Gans, 1925) of wave optics. For appropriately thin samples, the majority of the incident neutron beam is transmitted through the sample and the remaining neutrons are scattered only once before exiting the sample. The scattered intensity as a function of Q is independent of neutron wavelength and its shape near $Q = 0$ depends only on the particle dimensions. Fig. 1(*a*) represents a typical SANS scattering curve. The scattered intensity around $Q = 0$ cannot be measured directly because it lies in the same region as the transmitted beam, which is 10^3 to 10^7 times more intense than the scattered beam. Therefore, a beamstop is usually employed to prevent the transmitted beam from reaching and thus damaging the neutron detector. For any particle shape, the particle size can be described by its radius of gyration R_g or Guinier radius (Kostorz, 1979) which is the same as the radius of gyration in mechanics and is obtained from an analysis of the small-Q portion of the scattered-intensity curve. The range for which the Guinier analysis is valid is defined by $QR_g \leq \sim 1{\cdot}2$ (Kostorz, 1979). In addition, the ratio of the total scattering surface area to the volume of the sample in the neutron beam, S/V_b, can be obtained from an analysis of the large-Q portion of the scattered-intensity curve. In this region, the scattered intensity obeys the Q^{-4} Porod law (Kostorz, 1979). An equivalent spherical radius can be determined from the total scattering surface area.

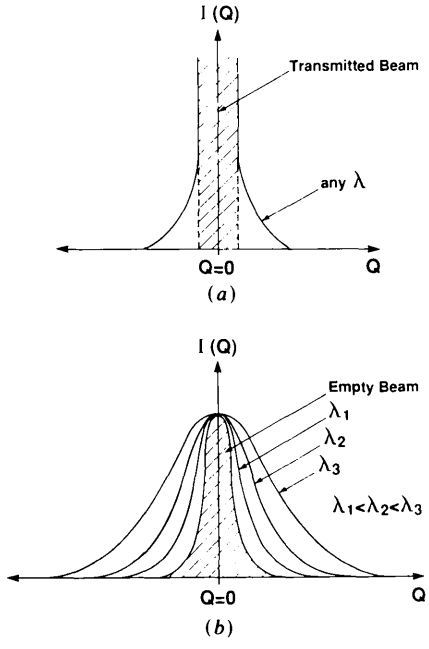

Fig. 1. (*a*) Representation of an $I(Q)$ *vs* Q scattered-intensity curve arising from conventional small-angle scattering, illustrating its wavelength-independent shape and the transmitted-beam region near $Q = 0$. (*b*) Representation of a typical set of $I(Q)$ *vs* Q multiple small-angle scattered-intensity curves from a single sample, illustrating their wavelength-dependent shape and the empty-beam curve.

At the opposite extreme, when $\nu \gg 1$ (the multiple refraction regime), every particle scatters and the scattered intensity is derived from geometrical optics (von Nardroff, 1926). The shape of the scattering curve is independent of the particle radius and depends only upon the difference in index of refraction between the scatterers and the matrix which, in turn, depends upon neutron wavelength as λ^2. This regime is not pursued further here.

When $\nu \simeq 1$ (the MSANS diffraction regime), the scattered intensity cannot be described by either conventional SANS diffraction or by multiple refraction. Scatterers with radii in the 0·1–10 μm range generally undergo phase shifts of the order of 1 for the range of neutron wavelengths usually available for SANS. Since larger particles scatter more intensely than smaller ones, the likelihood of multiple scattering becomes greater (Berk & Hardman-Rhyne, 1988). Furthermore, the incidence of coherent scattering *between* larger particles is greatly decreased, meaning that the single-particle scattering cross section does not contain a component due to interparticle interference. Thus, in the MSANS diffraction regime, multiple scattering arises solely from the statistical compounding of numerous coherent elastic single-particle scattering events in which interparticle interference does not play a significant role (Berk & Hardman-Rhyne, 1985).

A measure of the amount of incoherent multiple scattering is given by the parameter $\bar{z}$ (Berk & Hardman-Rhyne, 1988), which is the sample thickness, z, divided by the statistical neutron mean free path length, l.

$$\bar{z} = z/l = 1{\cdot}5\varphi z(\Delta\rho\lambda)^2 R, \tag{3}$$

where φ is the volume fraction of scatterers. $\bar{z}$ is

related to the sample transmission as $T_s = \exp\{-\bar{z}\}$. Since $\Delta\rho$ involves only coherent scattering lengths, $\bar{z}$ can only be calculated from the measured sample transmission after correcting for absorption and incoherent single-particle scattering, where applicable. A value of $\bar{z} = 0{\cdot}0$ means that there is no multiple scattering. In practice, the data from SANS samples of finite thickness such that $0 < \bar{z} \leq 1$ always contain some multiple scattering which is either negligibly small or treated as a small correction to the single-particle scattering. In MSANS measurements, the amount of multiple scattering is copious and $\bar{z}$ typically ranges from 10 to 400.

In the region of validity of MSANS, the intensity of the transmitted beam is immeasurably small and the width of the scattered intensity curve near $Q = 0$ is broadened far beyond the broadening due to instrumental resolution. The amount of beam broadening is dependent upon the incident neutron wavelength as illustrated in Fig. 1(*b*) where representative MSANS curves are shown for different wavelengths incident on a single sample. The intensities have been normalized such that $I(0) = 1{\cdot}0$. In each case, the scattered intensities, $I(Q)$, have a curvature, r_c, near $Q = 0$ and can be approximately described as a Gaussian with a width proportional to λ^2. For large Q, there is a crossover to single-scattering Porod behavior (Berk & Hardman-Rhyne, 1985), where the cross section is proportional to Q^{-4}.

It is evident from (1) and (3) that the contribution of incoherent multiple scattering to the total cross section depends upon a balance of the parameters which define ν and $\bar{z}$. For a given neutron-scattering contrast and wavelength, (3) indicates that the amount of multiple scattering depends linearly upon the sample thickness and the radii of the individual scatterers. Therefore, even though in practice thick samples (0·5-1·0 cm) are used to ensure copious multiple scattering, the MSANS formalism can also be applied to much thinner samples (0·1-0·2 cm) if the radii of the scatterers are sufficiently large. (From a practical standpoint, sample thickness can be chosen so that the wavelength dependence of the width of the scattering curve is easily observed within the range of available neutron wavelengths.)

Although the wavelength dependence at small Q seems to be the same as that for the multiple refraction regime, the underlying mechanism is different. When $\nu \simeq 1$, an effective radius, $R_{\text{eff}}(0)$, where the 0 refers to $Q = 0$, can be determined for the scatterers from the wavelength dependence of r_c using the MSANS formalism represented in equations (2.12)-(2.15) of Berk & Hardman-Rhyne (1985, 1988). The dimensionless parameter $r_c[QR] = r_c[Q]R$, where $[\ldots]$ means with respect to, is related to $\bar{z}$ *via* an empirical relation (Berk & Hardman-Rhyne, 1988)

$$r_c[QR] = 0{\cdot}926\{\bar{z}\ln^{0{\cdot}85}\bar{z}\}^{0{\cdot}5} \text{ for } \bar{z} > 5, \qquad (4)$$

which approximates the theory to better than 0·1% when $\bar{z} > 10$.

The MSANS formalism in effect replaces the standard Guinier analysis in the the small-Q region of $I(Q)$ where $R_{\text{eff}}(0)$, rather than R_g, defines the size of the scatterers. When polydispersity is present, $R_{\text{eff}}(0)$ can be written in terms of the moments of an assumed particle-size distribution. For the small-Q regime, $R_{\text{eff}}(0) = \langle R^4\rangle/\langle R^3\rangle$ (Berk & Hardman-Rhyne, 1985), where the brackets denote the arithmetic average of the argument. Note that in the low-$\bar{z}$ limit the MSANS formalism no longer applies and the moments are expressed in terms of the Guinier radius of gyration such that $R_g = [3\langle R^8\rangle/5\langle R^6\rangle]^{1/2}$ (Kostorz, 1979). If a similar relation for the effective radius can be found using the large-Q regime, then the average radius as well as the width of the size distribution can be found as shown below.

The standard Porod analysis (Kostorz, 1979) can be applied to the large-Q region of $I(Q)$. In this region, the scattered intensity can be written as

$$I(Q) = PQ^{-4} + B, \qquad (5)$$

where P is Porod's constant and B is a background term. The normalized total surface scattering area per unit volume, S/V_b, is determined directly from P. An effective pore radius, $R_{\text{eff}}(\infty)$, where ∞ refers to the large-Q regime, is calculated directly from S/V_b assuming spherical scatterers. For polydisperse systems, the moments of the size distribution are expressed as $R_{\text{eff}}(\infty) = \langle R^3\rangle/\langle R^2\rangle$. If both $R_{\text{eff}}(0)$ and $R_{\text{eff}}(\infty)$ are known, $\langle R\rangle$ as well as the width, β, of an assumed particle-size distribution can be determined.

To apply the MSANS formalism to the analysis of scattering from a system of spheres containing no internal structure, (3) and (4) indicate that the sample thickness, the scattering volume fraction (which is a refinable parameter), the scattering-length density and the wavelength dependence of r_c must be known in order to derive $R_{\text{eff}}(0)$. In addition, the constraints that $\bar{z} \geq 10$ and $0{\cdot}1 \leq \nu \leq 2$ must be satisfied. When $\nu > 2$, the scattering intensity falls into a crossover regime between diffraction and refraction. However, if $\bar{z}$ is sufficiently large, the MSANS formalism may even apply if $\nu > 2$ (Berk & Hardman-Rhyne, 1988).

The assumption that the scattering system is dominated by incoherent multiple scattering is extremely important since it means that the scattered intensity does not contain an interparticle interference term due to pair-pair correlations between particles. Since the scatterers are so large, *i.e.* comparable in size to the mean free path length of the neutrons, there is no coherent scattering between particles. Thus, even a dense system of scatterers may be considered dilute from the perspective of MSANS even though $\varphi/(1-\varphi) \sim \varphi$ does not apply.

Table 1. *Alumina samples prepared from Baikowski CR6, 6 $m^2 g^{-1}$ powder*

Sample	Thickness (cm)	Pore volume fraction, φ	%TD Volumetric	%TD MSANS
13-2	1·019	0·46	56·5	54
13-3	0·988	0·35	67·0	65
13-4	0·894	0·21	79·1	79
13-5	0·914	0·15	85·4	85
13-1	0·851	0·11	90·8	89
13-6	0·852	0·075	94·6	92·5
13-7	0·840	0·055	97·1	94·5
13-8	0·804	0·025	98·9	97·5

3. Alumina samples

The samples were prepared from Baikowski alumina powder (CR6, 6 $m^2 g^{-1}$), slipcast to an average green density of 53% of theoretical density (TD), where TD = 3·965 g cm^{-3}. The slip consisted of 43·5 vol.% alumina powder mixed into water along with 0·5 wt% of a polyelectrolyte dispersant (Darvan C). The suspension was ultrasonicated for 15 min and allowed to set overnight before being poured into molds with Teflon rings on top of plaster-of-paris blocks. After 55 min, the molds were removed from the blocks and sealed in a container overnight. The partially dried samples were then removed from the molds and sealed in containers for 2 d. The containers were then opened to the air for an additional 5–7 d before a series of oven-drying steps was performed as follows: 2 d at 337 K, 1 d at 354 K, 1 d at 375 K and 1 d at 389 K, after which a dry solid green body is obtained. In this fashion a family of eight nearly identical samples was prepared.

During sintering, samples were removed one by one at different times from the furnace to yield examples of material between 56·5 and 97·5% TD. The characteristics of the alumina samples are listed in Table 1. Sample densities measured volumetrically as well as those determined from the MSANS measurements are given. The sintering time-temperature curve is shown in Fig. 2. Each circle represents a sample removed from the furnace and the number alongside each circle is the measured %TD.

4. Neutron-scattering measurements

Measurements were made at the 20 MW research reactor at the National Institute of Standards and Technology (NIST). The NIST SANS facility (Glinka, 1981; Glinka, Rowe & LaRock, 1986) makes use of a velocity selector to choose the mean incident wavelength of the neutrons, λ, which have a wavelength spread $\Delta\lambda/\lambda = 0{\cdot}25$. Copious neutron fluxes can be obtained in the wavelength region between 5 and 20 Å due to a cryogenic moderator installed in the reactor core. The neutron beam is collimated with a 12 mm aperture which follows the velocity selector and an 8 mm aperture which precedes the sample position. Scattered neutrons are detected by a 64 × 64 cm position-sensitive detector divided into 128 × 128 pixels. The data are circularly averaged to produce one-dimensional intensity, $I(Q)$, *vs* Q curves. Intensities measured for Porod analysis were placed on an absolute scale by comparison with $I(Q)$ from a calibrated silica-gel sample measured under the same conditions.

The MSANS measurements were performed with no beamstop in front of the detector since the intense transmitted beam associated with conventional SANS measurements is absent. The absence of the beamstop ensures that the beam center can be found with high precision. With the center of the Gaussian precisely known, an accurate determination of the radius of curvature can be made. Measurement times ranged from 10 min to 1 h, depending upon the neutron wavelength. At the shortest wavelengths, the incident neutron beam is attenuated as needed in order to avoid saturating the detector. For a given wavelength, the broadest scattered intensity curves require the longest measuring times in order to accumulate sufficient counts.

5. Data analysis

5.1. *MSANS analysis*

MSANS measurements were performed on each sample at a minimum of five neutron wavelengths. The scattering curves exhibited the expected broadening with increasing neutron wavelength as shown in

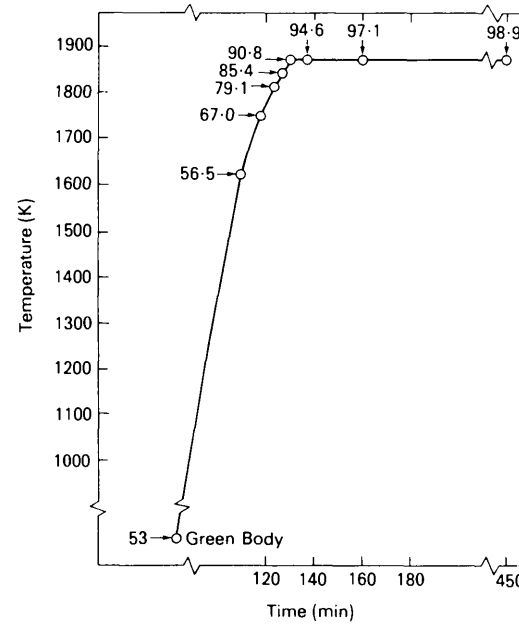

Fig. 2. Sintering time-temperature curve for the alumina samples. Each circle represents a sample removed from the furnace and the number alongside is the percent of theoretical density.

Fig. 3, where $I(Q)$ *vs* Q curves, normalized to $I(0) = 1{\cdot}0$, are plotted for the 85% TD sample. The features at $Q \leq 0{\cdot}005$ Å^{-1}, most obvious for the longer-wavelength data, are due to a change in detector sensitivity at the beam-center position. To avoid this region, Gaussian fits were made to each curve in the Q range beginning where the intensity is ~85-90% of $I(0)$ and extending to ~45% of $I(0)$. Below 40% of $I(0)$, the scattering curves did not fit well to a Gaussian.

For each curve fit, a radius of curvature is extracted from the standard deviation, σ, such that $r_c = (1/2\sigma)^{1/2}$. Blank spectra, measured at each wavelength with no scatterer in place, are also fitted to enable a correction for the instrument function (Hardman-Rhyne & Berk, 1985). Radii are extracted in each case from the empirical formula in (4) using (3) for $\bar{z}$. These values are averaged to obtain an effective radius, $R_{\text{eff}}(0)$, for the scatterers in each sample.

Finally, both $R_{\text{eff}}(0)$ and the scattering-volume fraction, φ, are refined simultaneously for each sample using a least-squares fitting method. Owing to the approximate nature of the empirical formula (4), the full numerical MSANS analysis describing r_c as a function of λ, developed in (2.12)-(2.15) of Berk & Hardman-Rhyne (1985), is used in the refinement procedure.

5.2. *Porod analysis*

The scattering at large Q was measured for each sample with an incident neutron wavelength of 6 Å and the detector offset to an angle of 3·5°. Sample transmissions were determined by dividing the total detector counts accumulated for each sample by the total detector counts accumulated under the same conditions with no sample in place. This method yields the equivalent of a single-scattering sample transmission. Values between 0·87 and 0·97 were measured, which fall within the range expected for Al_2O_3 when no multiple scattering is present.

Since the scattered intensity follows (5) in the Porod regime, both the Porod constant, P, and the background term, B, were found directly by making linear least-squares fits to IQ^4 *vs* Q^4 curves for each sample. The largest possible linear region of the curves was fit. In each case, the maximum Q value was 0·16 Å^{-1}, which is the largest Q value for which data were obtained. The minimum Q value ranged from 0·035 Å^{-1} for the 97·5% TD sample to 0·1 Å^{-1} for the 54% TD sample. The ratio of the normalized total scattering surface area to the volume of sample in the neutron beam S/V_b is determined directly from P. With the assumption of spherical scatterers, $R_{\text{eff}}(\infty)$ for the large-Q regime is also determined.

6. Results and discussion

The measured values of $r_c[Q]$ (symbols) are plotted *versus* λ in Fig. 4 along with the theoretical values (solid lines) determined using the MSANS formalism [(2.12)-(2.15) in Berk & Hardman-Rhyne (1985)]. As the scattering volume fraction decreases (*i.e.* the %TD increases), the calculated values of $R_{\text{eff}}(0)$ become

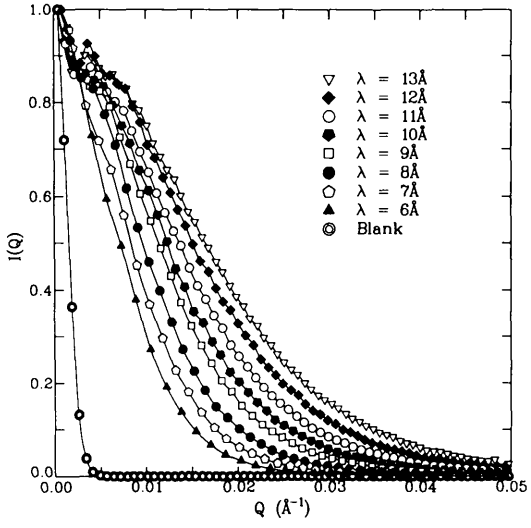

Fig. 3. Measured MSANS $I(Q)$ *vs* Q curves from the 85% TD alumina sample for eight neutron wavelengths. The curve for the empty-beam 'blank' was taken at $\lambda = 13$ Å.

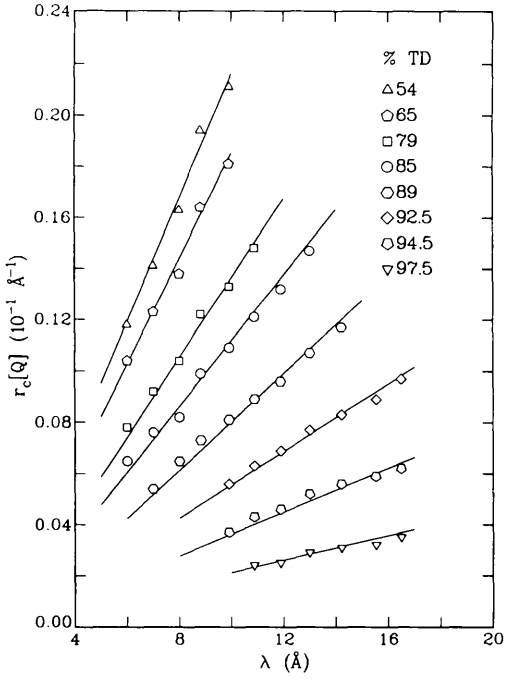

Fig. 4. Measured radii of curvature (symbols) and the corresponding MSANS theoretical fit (solid lines) as a function of neutron wavelength. The sample densities are those refined from the neutron-scattering measurements.

Table 2. *MSANS results*

Sample	%TD	Neutron wavelength λ (Å) Min.	Neutron wavelength λ (Å) Max.	Pore radius $R_{eff}(0)$ (μm)	$\bar{z}$ Min.	$\bar{z}$ Max.	Ratio* Min.	Ratio* Max.	Phase shift ν Min.	Phase shift ν Max.
13-2	54	6·0	9·9	0·20(1)	152	414	14	26	0·13	0·22
13-3	65	6·0	9·9	0·19(1)	98	289	11	21	0·12	0·21
13-4	79	6·0	10·9	0·170(5)	49	193	7	17	0·10	0·22
13-5	85	6·0	13·0	0·18(1)	32	204	6	17	0·09	0·28
13-1	89	7·0	14·2	0·23(2)	47	234	7	19	0·17	0·41
13-6	92·5	9·9	14·2	0·32(3)	96	298	11	21	0·35	0·66
13-7	94·5	9·9	16·5	0·53(5)	73	248	9	19	0·45	0·93
13-8	97·5	10·9	16·5	0·75(15)	40	126	6	13	0·53	1·10

* Ratio = $R_{eff}(0)/R_s(0)$, where $R_s(0)$ is the pore radius calculated assuming no multiple scattering is present.

much more sensitive to small changes in the volume fraction, φ. For example, an uncertainty of 0·01 on the value $\varphi = 0{\cdot}01$ has a much greater effect on $R_{eff}(0)$ than the same uncertainty on the value $\varphi = 0{\cdot}4$. In these cases, the refinement procedure was especially useful as it allowed the simultaneous determination of φ and $R_{eff}(0)$ values which best fit the r_c *vs* λ data. Values for the phase shift ν ranged from 0·1 to 1·0, as shown in Table 2, which fall well within the allowed range for MSANS analysis.

The slopes of the r_c *vs* λ curves are steepest for the intermediate-stage alumina samples, which have the largest pore volume fraction. These samples also have the largest $\bar{z}$ values and thus the largest amount of multiple scattering, even though the effective pore radii are smaller than those of the final-stage samples. In addition, the scattering intensities show beam broadening at smaller λ values and the width of the Gaussian at $Q = 0$ increases more rapidly with increasing λ.

When the pore volume fraction is small, as in the 97·5% TD sample, $\bar{z}$ is correspondingly smaller and the slope of the r_c *vs* λ curves is much flatter. Since the amount of multiple scattering is much less in the denser samples, the scattered intensities must be measured using longer-wavelength neutrons for beam broadening to be observed. Without the cryogenic moderator, copious neutron fluxes at wavelengths beyond ~12 Å would not be available and the most dense samples could not have been measured using the MSANS technique.

The refined value for the effective pore radius $R_{eff}(0)$, obtained from the data in Fig. 4, is listed for each sample in Table 2, along with the ranges of λ, $\bar{z}$ and ν. Also listed is the ratio of $R_{eff}(0)$ to the equivalent spherical radius $R_s(0)$ calculated assuming that no multiple scattering is present, *i.e.* using the standard Guinier analysis to obtain R_g and then assuming spherical scatterers to obtain $R_s(0)$.

The data points from Fig. 4 for all of the samples (circles) along with the empirical curve as given by (4) (solid line) are plotted as a function of $\bar{z}$ in Fig. 5. The dimensionless parameter $r_c[QR]$ is obtained by multiplying $r_c[Q]$ by the best $R_{eff}(0)$ value for each sample after refinement. The $\bar{z}$ values for these samples range from 40 to 400, well within the range of validity of the empirical formula. Thus, excellent agreement with (4) is expected.

A $\ln(I)$ *vs* $\ln(Q)$ plot of the Porod data (circles) for the 85% TD sample is shown in Fig. 6. The fitted background term [see (5)] of 0·018(1) cm^{-1} was subtracted prior to plotting. The solid line is the linear fit to $\ln(I)$ *vs* $\ln(Q)$ in the range $0{\cdot}055 \le Q \le 0{\cdot}155$ $Å^{-1}$, where the slope was determined to be −4·02(2). The effective pore radius, $R_{eff}(\infty)$, and the minimum Q value used for the Porod fit are listed in Table 3 for each sample, along with the normalized total scattering surface area, S/V_b. The normalized pore volume fraction $\varphi/(S/V_b)$ and the number of pores per unit sample volume, N/V_b, are also tabulated for each sample.

The $R_{eff}(0)$ and $R_{eff}(\infty)$ values calculated from the MSANS and Porod measurements, respectively, are plotted in Fig. 7, along with those obtained using

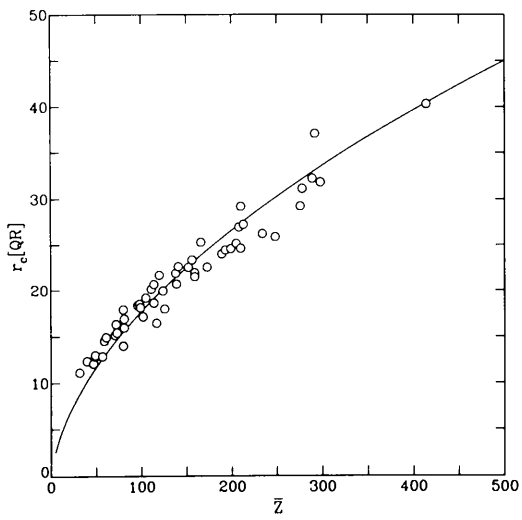

Fig. 5. Combined plot of $r_c[QR]$ *vs* $\bar{z}$ for all samples at all neutron wavelengths measured. The solid line is the empirical formula (4). The data points are the products of the measured $r_c[Q]$ and the best-fit value for the effective pore radius, $R_{eff}(0)$, for each sample.

mercury intrusion porosimetry (Rootare & Prenzlow, 1967) for the samples below 85% TD, where open porosity is expected. The MSANS determinations, which are weighted to the larger volume scatterers (Long & Krueger, 1989), indicate that the average pore radius for the distribution within the alumina is essentially flat, with a value of ~0·2 μm, in the intermediate sintering stage and increases sharply to ≥0·6 μm in the final stage. The large error bar on the value for the 97·5% TD sample is a consequence of the shallow slope in the r_c *vs* λ curve (Fig. 4). Since three local minima in the χ^2 fitting parameter were found for $R_{\text{eff}}(0)$ values between 0·6 and 0·9 μm, no single fit could be chosen as the 'best fit' to the MSANS formalism. An uncertainty in the pore volume fraction, φ, of approximately 0·005 was also found from the fitting procedure.

The $R_{\text{eff}}(\infty)$ values determined from the Porod analysis are weighted to the particles with the smallest scattering surface areas. Although consistently lower, the $R_{\text{eff}}(\infty)$ values agree qualitatively with the $R_{\text{eff}}(0)$ values. The average pore radius remains nearly constant at a value of ~0·1 μm throughout the intermediate stage and increases to ≥0·4 μm in the final stage. The large error bar on $R_{\text{eff}}(\infty)$ for the 97·5% TD sample is mainly due to the uncertainty in φ as determined from the MSANS analysis.

The porosimetry results agree qualitatively with results obtained from both the MSANS and Porod analyses for intermediate-stage sintering. The observed quantitative discrepancies are expected since the MSANS and Porod radii are derived from a measure of all of the voids in the system, with MSANS radii weighted to the larger-volume and Porod radii weighted to the smaller-volume voids. On the other hand, the porosimetry radii mainly represent the size of the small necks between pores.

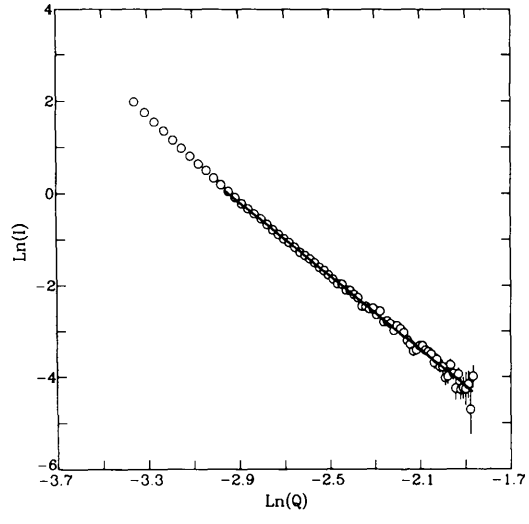

Fig. 6. Porod data for the 85% TD sample plotted on a ln (I) *vs* ln (Q) scale after subtraction of the fitted background term [see (5)]. The solid line is the linear least-squares fit to the data in the range $0{\cdot}055 \leq Q \leq 0{\cdot}155$ Å^{-1}. The fitted slope is −4·02(2).

Mercury intrusion porosimetry assumes that the largest pores are on the outside of the sample. This is important because the pressure required to fill a large pore is less than that required to fill a small pore. However, as the mercury penetrates a homogeneous sample consisting of a random distribution of necks and larger channel-like voids, a significant number of necks may be encountered before the mercury reaches the open channels. Since the neck size is measured at a higher pressure than that required for the open channel, the mercury reaches the channel after the appropriate pressure to measure its size has been exceeded. Thus, large voids in the interior of a sample may not be measured, even if they form a majority population.

The MSANS and Porod results for pore size assume spherical scatterers whereas the porosimetry results are obtained assuming cylindrical pore morphology. Yet the same trend in the evolution of the effective pore radius during intermediate stage sintering is reported in each case. This occurs because the average length of the cylindrical channels is ≥10 μm, which is beyond the measurable range of even the MSANS technique. Thus, the pore channels can be effectively represented by strings of spheres, with $R_{\text{eff}}(0)$ and $R_{\text{eff}}(\infty)$ corresponding to the cross-sectional radii of the cylinders. $R_{\text{eff}}(0)$ is dominated by the larger-diameter and $R_{\text{eff}}(\infty)$ by the smaller-diameter channels in the size distribution.

The important result of the MSANS, Porod and porosimetry measurements is that the effective pore radius remains constant through the intermediate stage of sintering. This is consistent with topological decay models of the intermediate sintering stage in which an interconnected pore network decays in a stable manner (Rhines & DeHoff, 1984). Throughout this stage, the network of interconnected channels decays such that the ratio $\varphi/(S/V_b)$, or pore volume fraction to surface area per unit volume of sample in the neutron beam, remains constant (DeHoff, Rummel, LaBuff & Rhines, 1966). Consequently, the pore channels become fewer while retaining a constant diameter as densification proceeds. This can easily be observed in Tables 2 and 3, which show constant $R_{\text{eff}}(0)$, $R_{\text{eff}}(\infty)$ and $\varphi/(S/V_b)$ values for the intermediate-sintering-stage samples. Also shown is the number of pores per unit sample volume (N/V_b), which decreases sharply, as expected, as intermediate-stage sintering progresses.

Before the channels have disappeared altogether, a transition into the final sintering stage occurs in which the porosity becomes isolated. Pore isolation occurs because the channels rupture or 'pinch off' when they can no longer maintain their length while at the same time remaining stable against the increas-

Table 3. *Porod results*

Sample	%TD	Q_{min} (Å^{-1})	Pore radius $R_{eff}(\infty)$ (μm)	Normalized surface area S/V_b* (×10^4 cm^{-1})	Normalized pore volume fraction $\varphi/(S/V_b)$ (×10^{-6} cm)	Number of pores per unit volume N/V_b (×10^{12} cm^{-3})
13-2	54	0·10	0·091(1)	15·2(2)	3·03(4)	147·0(27)
13-3	65	0·09	0·108(1)	9·7(1)	3·60(4)	66·0(5)
13-4	79	0·07	0·108(1)	5·83(3)	3·60(2)	39·6(48)
13-5	85	0·065	0·120(1)	3·74(2)	4·01(2)	20·5(18)
13-1	89	0·055	0·154(1)	2·15(1)	5·12(2)	7·2(10)
13-6	92·5	0·045	0·185(1)	1·22(1)	6·16(3)	2·84(72)
13-7	94·5	0·04	0·298(2)	0·553(3)	9·93(4)	0·495(5)
13-8	97·5	0·035	0·44(9)	0·1623(4)	14·5(29)	0·08(3)

* S/V_b is the ratio of the total scattering surface area to the volume of the sample in the neutron beam, where the beam diameter is 0·9 cm.

ing sintering force (Rhines & DeHoff, 1984). The isolated pores become more spherical, achieving radii which are greater than the cross-sectional radii of the original channels, yet are still within the MSANS range. As the number of isolated pores increases, their larger dimension increasingly contributes to the total scattering, until it finally dominates the measured MSANS intensities. Thus, as seen in Tables 2 and 3, $R_{eff}(0)$ and $R_{eff}(\infty)$ begin increasing gradually as the transition from intermediate to final-stage sintering begins. Late in the final sintering stage, a more rapid increase in both $R_{eff}(0)$ and $R_{eff}(\infty)$ is observed as the microstructure becomes dominated by isolated pores.

7. Concluding remarks

The multiple small-angle neutron-scattering technique was successfully used to observe the transition from one sintering stage to another in the densification of alumina. The effective radius of the pore-size distribution, as measured by MSANS, Porod scattering and mercury porosimetry, remained constant throughout the intermediate stage of sintering, with a rapid increase measured by MSANS and Porod scattering as densification proceeds beyond 85% of theoretical density. These results are consistent with sintering models which equate the intermediate stage with the stable decay of a topological network of channels and junction pores in the system. Before complete densification can occur, a transition into the final sintering stage takes place in which the porosity forms isolated spherical voids. The Porod and MSANS results for the radii of the final-stage voids agree qualitatively, indicating that the pore-size distribution does not broaden appreciably as its peak advances toward higher R values during late-stage densification.

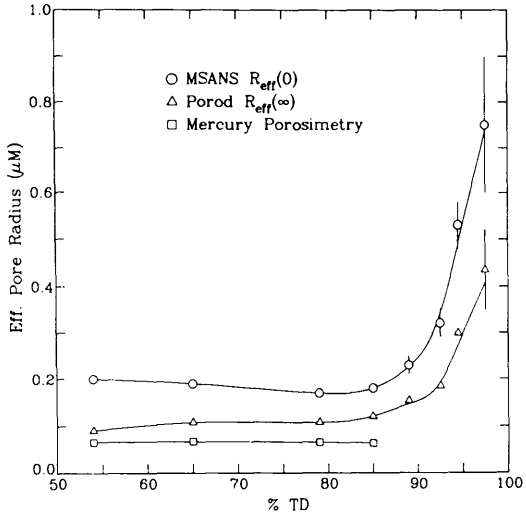

Fig. 7. Effective pore radii for the alumina samples as a function of percent theoretical density determined from the MSANS formalism from a Porod analysis and from mercury porosimetry measurements on the samples below 85% TD, where open porosity is expected.

The agreement among the MSANS, Porod and porosimetry results concerning the constant value of the pore radius during the intermediate stage illustrates that the MSANS formalism, as applied to the alumina system, is adaptable to the use of strings of spheres to describe cylindrical pore channels and is thus not limited by the restriction of isolated spherical scatterers. The quantitative differences between the scattering and the porosimetry results arise because the MSANS and Porod radii are derived from a measure of all of the voids in the system, with MSANS radii weighted toward the larger and Porod radii weighted toward the smaller voids. However, in a system consisting of a homogeneous distribution of pore sizes, such as alumina, the porosimetry radii are dominated by the size of the small necks between pore channels.

As densification proceeds beyond 85% TD, the channels become pinched off and then the transition from an open pore network to isolated pores occurs, resulting in an increase in both $R_{eff}(0)$ and $R_{eff}(\infty)$. Although even the largest pores are expected to begin to shrink by 95% TD (Johnson, 1990), the scattering results (Fig. 7) indicate that $R_{eff}(0)$ and $R_{eff}(\infty)$ may

still be increasing at 97·5% TD. This suggests that discontinuous grain growth may be taking place. However, the large uncertainties in the scattering volume fraction, φ, and the effective radii, $R_{\rm eff}(0)$ and $R_{\rm eff}(\infty)$, preclude drawing firm conclusions.

Although the final-stage samples were originally intended for single-scattering SANS measurements, it was found that even the 97·5% TD sample was within the limit of applicability of the MSANS technique. There was significant wavelength-dependent beam broadening and even the smallest $\bar{z}$ value ($\bar{z}$ = 40) is well within the MSANS formalism. However, the fact that φ is so small means that the change in r_c as a function of λ is small (see Fig. 4). This nearly flat slope makes the refinement procedure difficult, resulting in large uncertainties in the fitted $R_{\rm eff}(0)$ and φ values. To improve the determination of $R_{\rm eff}(0)$ during final-stage sintering, measurements of the higher-density samples are planned with a high-resolution small-angle X-ray scattering instrument (Long, Jemian, Weertman, Black, Burdette & Spal, 1991). This instrument can measure the single-scattering intensities from pores 4·0 nm to 1·0 μm in size and thus bridge the gap between those sizes which can be easily measured by conventional SANS and MSANS techniques.

This work was supported in part by the US Army Research Office under contract no. MIPR ARO 102-90 and in part by the Department of Energy under grant no. DE-FG05-84ER45063.

References

BERK, N. F. & HARDMAN-RHYNE, K. A. (1985). *J. Appl. Cryst.* **18**, 467-472.

BERK, N. F. & HARDMAN-RHYNE, K. A. (1988). *J. Appl. Cryst.* **21**, 645-651.

COBLE, R. L. (1961). *J. Appl. Phys.* **32**, 787-792, 793-799.

DEHOFF, R. T., RUMMEL, R. A., LABUFF, H. P. & RHINES, F. N. (1966). *Modern Developments in Powder Metallurgy*, edited by H. H. HAUSNER, Vol. 1, pp. 310-331. New York: Plenum Press.

GANS, R. (1925). *Ann. Phys. (Leipzig)*, **76**, 29-38.

GLINKA, C. J. (1981). *Neutron Scattering. AIP Conf. Proc.* No. 89, pp. 395-397.

GLINKA, C. J., ROWE, J. M. & LAROCK, J. G. (1986). *J. Appl. Cryst.* **19**, 427-439.

HARDMAN-RHYNE, K. A. & BERK, N. F. (1985). *J. Appl. Cryst.* **18**, 473-479.

JOHNSON, D. L. (1990). Private communication.

KINGERY, W. D. & BERG, M. (1955). *J. Appl. Phys.* **26**, 1205-1212.

KOSTORZ, G. (1979). *A Treatise on Materials Science and Technology*, edited by H. HERMAN, Vol. 15, pp. 227-289. New York: Academic Press.

LONG, G. G., JEMIAN, P. R., WEERTMAN, J. R., BLACK, D. R., BURDETTE, H. E. & SPAL, R. (1991). *J. Appl. Cryst.* **24**, 30-37.

LONG, G. G. & KRUEGER, S. (1989). *J. Appl. Cryst.* **22**, 539-545.

NARDROFF, R. VON (1926). *Phys. Res.* **28**, 240-246.

POROD, G. (1951). *Kolloid Z.* **124**, 83-114.

RAYLEIGH, J. W. LORD (1910). *Proc. R. Soc. London Ser. A*, **84**, 25-46.

RAYLEIGH, J. W. LORD (1914). *Proc. R. Soc. London Ser. A*, **90**, 219-225.

RHINES, F. N. & DEHOFF, R. T. (1984). *Sintering and Heterogeneous Catalysis, Materials Science Research*, edited by G. C. KUCZYNSKI, A. E. MILLER & G. A. SARGENT, Vol. 16, pp. 49-61. New York: Plenum Press.

ROOTARE, H. M. & PRENZLOW, C. F. (1967). *J. Phys. Chem.* **71**, 2733-2736.

WEISS, R. J. (1951). *Phys. Rev.* **83**, 379-389.

SHORT COMMUNICATIONS

Contributions intended for publication under this heading should be expressly so marked; they should not exceed about 1000 *words; they should be forwarded in the usual way to the appropriate Co-editor; they will be published as speedily as possible.*

Acta Cryst. (1991). A**47**, 290-292

Rank 0, 1, 2 and 3 magnetic and non-magnetic physical-property tensors.

By S. Y. LITVIN* and D. B. LITVIN, *Department of Physics, The Pennsylvania State University, The Berks Campus, PO Box* 7009, *Reading, PA* 19610-6009, *USA*

(*Received* 11 *September* 1990; *accepted* 12 *December* 1990)

Abstract

The form of 36 rank 0, 1, 2 and 3 magnetic and non-magnetic physical-property tensors invariant under each of the 236 subgroups of $6(Z)/M(Z)M(X)M(1)1'$ ($D_{6h}1'$) and each of the 420 subgroups of $M(Z)\bar{3}(XYZ)M(XY)1'$ (O_h1') is tabulated.

* Mailing address: 1701 Bern Road, Apartment B2, Wyomissing, PA 19610, USA.

0108-7673/91/030290-03$03.00

1. Introduction

A vast amount of literature exists on the derivation and tabulation of the form of physical-property tensors invariant under the non-magnetic crystallographic point groups (Jahn, 1949; Nye, 1957; Birss, 1964; Wooster, 1973; Kopsky, 1979*a*; Fumi & Ripamonti, 1980; Sands, 1982; and references contained in these sources). A wide variety of tensors and their physical interpretation is given by Sirotin & Shaskolskaya (1975). Recently, a computer-based